Quantitative phase-contrast tomography of a liquid phantom using a conventional x-ray tube source

Julia Herzen[1], Tilman Donath[2], Franz Pfeiffer[2,3,*], Oliver Bunk[2], Celestino Padeste[2], Felix Beckmann[1], Andreas Schreyer[1], and Christian David[2]

[1]*GKSS Research Centre, 21502 Geesthacht, Germany*
[2]*Paul Scherrer Institut, 5232 Villigen PSI, Switzerland*
[3]*Ecole Polytechnique Fédérale de Lausanne, 1015 Lausanne, Switzerland*
[*]*Present address: Department of Physics, Technical University Munich, 85747 Garching, Germany*
julia.herzen@gkss.de

Abstract: Over the last few years, differential phase-contrast x-ray computed tomography (PC-CT) using a hard x-ray grating interferometer and polychromatic x-ray tube sources has been developed. The method allows for simultaneous determination of the attenuation coefficient and the refractive index decrement distribution inside an object in three dimensions. Here we report experimental results of our investigation on the quantitativeness and accuracy of this method. For this study, a phantom consisting of several tubes filled with chemically well-defined liquids was built and measured in PC-CT. We find, that the measured attenuation coefficients and refractive index decrements closely match calculated, theoretical values. Moreover, the study demonstrates, how substances with similar attenuation coefficient or refractive index decrement, can be uniquely distinguished by the simultaneous, quantitative measurement of both quantities.

OCIS codes: (110.7440) X-ray imaging; (110.6955) Tomographic imaging; (110.3175) Interferometric imaging.

References and links

1. A. Momose, "Phase-sensitive imaging and phase tomography using X-ray interferometers," Opt. Express **11,** 2303–2314 (2003).
2. A. Momose, "Recent advances in X-ray phase imaging," Jpn. J. Appl. Phys. **44,** 6355–6367 (2005).
3. F. Beckmann, K. Heise, B. Kölsch, U. Bonse, M. F. Rajewsky, M. Bartscher, and T. Biermann, "Three-Dimensional Imaging of Nerve Tissue by X-Ray Phase-Contrast Microtomography," Biophys. J. **76,** 98-102 (1999).
4. P. Cloetens, W. Ludwig, J. Baruchel, D. van Dyck, J. van Landuyt, J. P. Guigay, and M. Schlenker, "Holotomography: Quantitative phase tomography with micrometer resolution using hard synchrotron radiation x rays," Appl. Phys. Lett. **75,** 2912–2914 (1999).
5. T. E. Gureyev, C. Raven, A. Snigirev, I. Snigireva, and S. W. Wilkins, "Hard x-ray quantitative non-interferometric phase-contrast microscopy," J. Phys. D **32,** 563-567 (1999).
6. T. Weitkamp, A. Diaz, C. David, F. Pfeiffer, M. Stampanoni, P. Cloetens, and E. Ziegler, "X-ray phase imaging with a grating interferometer," Opt. Express **12,** 6296–6304 (2005).
7. U. Bonse, F. Busch, O. Günnewig, F. Beckmann, R. Pahl, G. Delling, M. Hahn, and W. Graeff, "3D computed X-ray tomography of human cancellous bone at 8 m," Bone and Miner. **25,** 25–38 (1994).
8. A. Momose, "Demonstration of phase-contrast X-ray computed tomography using an X-ray interferometer," Nucl. Instrum. Method A **352,** 622–628 (1995).

#108621 - $15.00 USD Received 11 Mar 2009; revised 18 Apr 2009; accepted 30 Apr 2009; published 29 May 2009

9. F.A. Dilmanian, Z. Zhong, B. Ren, X.Y. Wu, L.D. Chapman, I. Orion, and W.C. Thomlinson, "Computed tomography of x-ray index of refraction using the diffraction enhanced imaging method," Phys. Med. Biol. **45,** 933–946 (2000).
10. K. A. Nugent, T. E. Gureyev, D. F. Cookson, D. Paganin, and Z. Barnea, "Quantitative phase imaging using hard X rays," Phys. Rev. Lett. **77,** 2961–2964 (1996).
11. T. Koyama, H. Takano, Y. Tsusaka, and Y. Kagoshima, "Tomographic quantitative phase measurement by hard X-ray micro-interferometer with 250 nm spatial resolution," Spectrochim. Acta Part B **62,** 603–607 (2007).
12. P. J. McMahon, A. G. Peele, D. Paterson, J. J. A. Lin, T. H. K. Irving, I. McNulty, and K. A. Nugent, "Quantitative X-ray phase tomography with sub-micron resolution," Optics Communications **217,** 53–58 (2003).
13. G. R. Myers, S. C. Mayo, T. E. Gureyev, D. M. Paganin, and S. W. Wilkins, "Polychromatic cone-beam phase-contrast tomography," Phys. Rev. A (Atomic, Molecular, and Optical Physics) **76,** 045804 (2007).
14. S. C. Mayo, P. R. Miller, S. W. Wilkins, T. J. Davis, D. Gao, T. E. Gureyev, D. Paganin, D. J. Parry, A. Pogany, and A. W. Stevenson, "Quantitative X-ray projection microscopy: phase-contrast and multi-spectral imaging," J. Microsc. **207,** 79–96 (2001).
15. S.C. Mayo, T.J. Davis, T.E. Gureyev, P.R. Miller, D. Paganin, A. Pogany, A.W. Stevenson, and S.W. Wilkins, "X-ray phase-contrast microscopy and microtomography," Opt. Express **11,** 2289–2302 (2003).
16. F. Pfeiffer, C. Kottler, O. Bunk, and C. David, "Hard X-Ray Phase Tomography with Low-Brilliance Sources," Phys. Rev. Lett. **98,** 108105 (2007).
17. F. Pfeiffer, O. Bunk, C. Kottler, and C. David, "Tomographic reconstruction of three-dimensional objects from hard X-ray differential phase contrast projection images," Nucl. Instrum. Methods Phys. Res. A **580,** 925–928 (2007).
18. M. Engelhardt, J. Baumann, M. Schuster, C. Kottler, F. Pfeiffer, O. Bunk, and C. David, "High-resolution differential phase contrast imaging using a magnifying projection geometry with a microfocus x-ray source," Appl. Phys. Lett. **90,** 224101 (2007).
19. F. Pfeiffer, T. Weitkamp, O. Bunk, and C. David, "Phase retrieval and differential phase-contrast imaging with low-brilliance X-ray sources," Nature Phys. **2,** 258 (2006).
20. C. Kottler, F. Pfeiffer, O. Bunk, C. Grünzweig, J. Bruder, R. Kaufmann, T. Tlustos, H. Walt, I. Briod, T. Weitkamp, and C. David, "Phase contrast X-ray imaging of large samples using an incoherent laboratory source," Phys. Status Solidi A **204,** 2728–2733 (2007).
21. A. C. Kak and M. Slaney, "Principles of Computerized Tomography," IEEE Press, New York (1987).
22. J. Als-Nielsen, "Elements of Modern x-ray Physics," John Wiley & Sons, Chichester (2008).
23. D. M. Paganin, "Coherent x-ray Optics," Oxford University Press, New York (2006).
24. R. W. James, "The optical principles of the diffraction of x-rays," (1962).
25. C. David, J. Bruder, T. Rohbeck, C. Grünzweig, C. Kottler, A. Diaz, O. Bunk, and F. Pfeiffer, "Fabrication of diffraction gratings for hard X-ray phase contrast imaging," Microelectron. Eng. **84,** 1172-1177 (2007).
26. D. R. Lide, "CRC Handbook of Chemistry and Physics (60th Edition)," Taylor and Francis, Boca Raton, FL (1980).
27. For the calculation of δ_c the tabulated values of f^1 from L. Kissel for elastic photon-atom scattering, anomalous scattering factors were taken from the file f1f2_asf_Kissel.dat of the DABAX library [28].
28. DABAX library, http://ftp.esrf.eu/pub/scisoft/xop2.3/DabaxFiles.
29. E. F. Plechaty, D. E. Cullen, and R. J. Howerton, "Tables and graphs of photon-interaction cross sections from 0.1 keV to 100 MeV derived from the LLL evaluated-nuclear-data library," Lawrence Livermore National Laboratory (1981).
30. B. D. Arhatari, K. Hannah, E. Balaur, and A. G. Peele, "Phase imaging using a polychromatic X-ray laboratory source," Opt. Express **16 (24),** 19950–19956 (2008).
31. M. Engelhardt, C. Kottler, O. Bunk, C. David, C. Schroer, J. Baumann, M. Schuster, and F. Pfeiffer, "The fractional Talbot effect in differential x-ray phase-contrast imaging for extended and polychromatic x-ray sources," J. Microsc. **232 (1),** 145–157 (2008).

1. Introduction

Phase-contrast x-ray imaging techniques are used to increase contrast in weakly absorbing biological samples [1, 2]. For a long time, phase-contrast computed tomography (CT) could only be performed using highly brilliant synchrotron radiation sources [1, 2, 3, 4, 5, 6]. Quantitative measurements were reported [7, 8, 9, 10, 11, 12, 13] and even verified in a few cases using sychrotron radiation in combination with diffraction enhanced imaging (DEI) [9], propagation-based phase-contrast imaging [10], and phase-contrast microscopy using zone plates [11, 12].

Recently, the use of laboratory x-ray sources for phase-contrast imaging became feasible and has been demonstrated to provide excellent results for both microscopic specimens using phase

#108621 - $15.00 USD Received 11 Mar 2009; revised 18 Apr 2009; accepted 30 Apr 2009; published 29 May 2009

propagation techniques [13, 14, 15] and macroscopic specimens using the grating interferometer approach [16, 17, 18, 19, 20]. This work is particularly based on the grating interferometer approach that is compatible with low-brilliance x-ray sources. Here we present experimental results of a study on the quantitativeness and accuracy of the reconstructed three-dimensional distribution of the attenuation coefficients and refractive index decrements in a self-built phantom. The present work was largely motivated by the fact that modern medical CT applications increasingly rely on a quantitative interpretation of the tomographic gray-scale images, e.g., in the assessment of bone density in the context of osteoporosis.

2. Materials and methods

The refractive index of a three-dimensional object can be described by its complex refractive index distribution $n(x,y,z) = 1 - \delta(x,y,z) + i\beta(x,y,z)$, where x, y, and z describe the coordinate system of the sample. In conventional absorption-contrast CT the imaginary part β is measured in form of the linear attenuation coefficient of the x-rays. A combination of the Radon transform of the object with Beer-Lambert's law describes the transmission projection in one plane $z = z_0$ [21, 22]

$$T^{\Theta}(x') = \exp\left[-\int_0^d \frac{4\pi}{\lambda}\,\beta(x',y')\mathrm{d}y'\right] = \exp\left[-\int_0^d (x',y')\mathrm{d}y'\right], \tag{1}$$

where $(x',y') = 4\pi/\lambda \cdot \beta(x',y')$, λ is the x-ray wave length, and x' and y' belong to a coordinate system which is rotated by the projection angle Θ around the z-axis with respect to x and y. Integration is carried out along the x-ray path over the extension of the sample of diameter d. Note that we have omitted the variable z to simplify the writing. The mass attenuation coefficient ($/\rho$) is defined by the ratio of the linear attenuation coefficient and density ρ. For mixtures that consist of I components, each with mass attenuation coefficient ($/\rho)_i$, with $i = 1,...,I$, the resulting mass attenuation coefficient is given by

$$\left(\frac{}{\rho}\right)_{subst} = \sum_{i=1}^{I} \left(\frac{}{\rho}\right)_i W_i, \tag{2}$$

where W_i is the weight fraction of the i-th component and the resulting linear attenuation coefficient simply is $_{subst} = (\ /\rho)_{subst} \cdot \rho_{subst}$, with the density of the substance ρ_{subst}.

In differential phase-contrast imaging, the variations of the real part of the refractive index $1-\delta$ of the object are detected by analyzing the slight refraction of x-rays caused by the object. In addition to the absorption-contrast projection in Eq. (1), we measure the differential phase-contrast projection of refraction angles [23]

$$\alpha^{\Theta}(x') = \frac{\lambda}{2\pi}\,\frac{\partial\Phi^{\Theta}(x')}{\partial x'} = \int_0^d \frac{\partial\delta(x',y')}{\partial x'}\mathrm{d}y', \tag{3}$$

where $\Phi^{\Theta}(x') = 2\pi/\lambda \int_0^d \delta(x',y')\mathrm{d}y'$ is the spatially dependent, total relative phase shift of the x-ray wave front acquired during its propagation through the sample.

The refractive index decrement δ depends on the x-ray wavelength λ and on the density of the sample as [24]

$$\delta_{subst} = \frac{r_e\lambda^2}{2\pi}\sum_{i=1}^{I} N_i f_i^1, \tag{4}$$

where $r_e = 2.82\cdot 10^{-15}$m is the classical electron radius, N_i is the atomic density of type i atoms given as atoms per unit volume, and f_i^1 is the real part of their atomic scattering factor in the

#108621 - $15.00 USD Received 11 Mar 2009; revised 18 Apr 2009; accepted 30 Apr 2009; published 29 May 2009

forward direction. If the photon energy of the incident x-ray radiation lies considerably above the absorption edges, we may put $f_i^1 = Z_i$, the total number of electrons in the atom and the sum in Eq. (4) then describes the electron density inside the sample. To obtain δ from given elemental weight fractions W_i, we substitute $N_i = (W_i \cdot N_A/A_i)\rho_{subst}$, with the atomic mass A_i of atom i and the Avogadro's number N_A, into Eq. (4).

For the reconstruction of the object's original complex refractive index distribution, or more explicitly of (x,y) and $\delta(x,y)$, from the two sets of projection images $T^\Theta(x')$ and $\alpha^\Theta(x')$, respectively, a filtered back-projection reconstruction algorithm is usually applied [21]. For the transmission projections $T^\Theta(x')$ in Eq. (1) the corresponding filtered back-projection reconstruction can be written as [21, Chapter 3, Eq. (31)]

$$(x,y) = -\int_0^\pi \mathscr{F}^{-1}\left\{\mathscr{F}\left[lnT^\Theta(\omega)\right]\cdot\mathscr{F}\left[k(\omega)\right]\right\}\mathrm{d}\Theta, \tag{5}$$

where $\mathscr{F}\left[lnT^\Theta(\omega)\right]$ represents the Fourier transform of the logarithm of the normalized transmission projection, $\mathscr{F}^{-1}$ denotes the inverse Fourier transform operator, and $\mathscr{F}\left[k(\omega)\right] \equiv |\omega|$ is the Fourier representation of the filter function for line projection integrals.

The reconstruction of $\delta(x,y)$ from the differential phase-contrast projections $\alpha^\Theta(x')$ in Eq. (3) is achieved as [16, 21]

$$\delta(x,y) = \int_0^\pi \mathscr{F}^{-1}\left\{\mathscr{F}\left[\alpha^\Theta(\omega)\right]\cdot\mathscr{F}\left[h(\omega)\right]\right\}\mathrm{d}\Theta, \tag{6}$$

where $\mathscr{F}\left[\alpha^\Theta(\omega)\right]$ represents the Fourier transform of the projections of the measured deflection angles and $\mathscr{F}\left[h(\omega)\right] = i\cdot\mathrm{sgn}(\omega)/(2\pi)$ is the Fourier transform of the filter function for gradient projections, where here $\mathrm{sgn}(\omega)$ is the sign function. Please note that for a correct reconstruction of the phase signal the approximation of a weakly scattering sample was made [23]. Since the presence of a strong scatterer will completely destroy the interference pattern of the grating interferometer, this approximation can be considered as fulfilled when a differential phase contrast can be measured. In a fan-beam setup the sensitivity of the grating interferometer is reduced by the factor r_1/l [18, Eq. (8)], where r_1 is the source-to-sample distance and l is the source-to-G1 distance. To correct for this effect, the recorded phase projections were renormalized by multiplication with $(r_1/l)^{-1}$ = [(1.4 m - 0.078 m)/(1.4 m)]$^{-1}$ = 1.059 prior to reconstruction.

We built a phantom consisting of thirteen small cylindrical low-density polyethylene (PE-LD) tubes with an outer diameter of 8 mm and a volume of 0.5 ml that we filled with fluids of well defined chemical composition (compare Table 1). To cover a wide range of attenuation coefficients and refractive index decrements, we mixed different pure liquids (ethanol, water, glycerol) and salts (NaI, NaCl).

Differential phase-contrast x-ray imaging and CT was carried out at the Laboratory for Micro- and Nanotechnology, Paul Scherrer Institut, Switzerland, using an x-ray grating interferometer as schematically shown in Fig. 1. The interferometer consists of a source grating G0, a phase grating G1, and an analyzer absorption grating G2. The source grating G0, which is placed close to the x-ray tube anode, allows for the use of x-ray sources with square-millimeter-sized focal points [19]. The signal is formed within the two gratings G1 and G2 due to the Talbot self-imaging effect [23]. The interferometer that was used here was designed for an x-ray energy of 28 keV and consisted of three gratings with respective periods of p_0 = 14.2 m, p_1 = 3.5 m, and p_2 = 2.0 m and respective structure heights of h_0 = 42 m, h_1 = 36 m, and h_2 = 26 m. The distance between G_0 and G_1 was 1.40 m and the distance between G_1 and G_2 was 0.198 m, corresponding to the fifth fractional Talbot distance. The gratings were produced

#108621 - $15.00 USD Received 11 Mar 2009; revised 18 Apr 2009; accepted 30 Apr 2009; published 29 May 2009

Table 1. Density and elemental composion of the fluids. These values were used in the calculation of Δ_c and $\Delta\delta_c$ listed in Table 2.

			Elemental weight fraction W_i					
Solution [wt.%]	**Identifier**	**Density** [g/cm^3]	H [wt.%]	O [wt.%]	C [wt.%]	Na [wt.%]	Cl [wt.%]	I [wt.%]
H_2O (demineralized)	H_2O	0.9982	11.19	88.81	–	–	–	–
glycerol (99.5%)	Gly	1.26	8.76	52.12	39.13	–	–	–
ethanol (p.a. 99.9%)	EtOH	0.7894	13.13	34.73	52.14	–	–	–
H_2O+NaCl 1.25%	H_2O-NaCl1.25	1.0072	11.05	87.70	–	0.49	0.76	–
H_2O+NaCl 2.5%	H_2O-NaCl2.5	1.0160	10.91	86.59	–	0.98	1.52	–
H_2O+NaCl 5%	H_2O-NaCl5	1.0340	10.63	84.37	–	1.97	3.03	–
H_2O+NaCl 10%	H_2O-NaCl10	1.0707	10.07	79.93	–	3.93	6.07	–
ethanol+NaI 1.25%	EtOH-NaI1.25	–	12.96	34.29	51.49	0.19	–	1.06
ethanol+NaI 2.5%	EtOH-NaI2.5	–	12.80	33.86	50.84	0.38	–	2.12
ethanol+NaI 5%	EtOH-NaI5	–	12.47	32.99	49.54	0.77	–	4.23
ethanol (75%) + glycerol (25%)	EtOH75-Gly25	–	–	–	–	–	–	–
ethanol (50%) + glycerol (50%)	EtOH50-Gly50	–	–	–	–	–	–	–
ethanol (25%) + glycerol (75%)	EtOH25-Gly75	–	–	–	–	–	–	–

on 4 inch silicon wafers in a fabrication process involving photolithography, deep etching into silicon, and (for the absorption gratings G0 and G2) electroplating of gold [25].

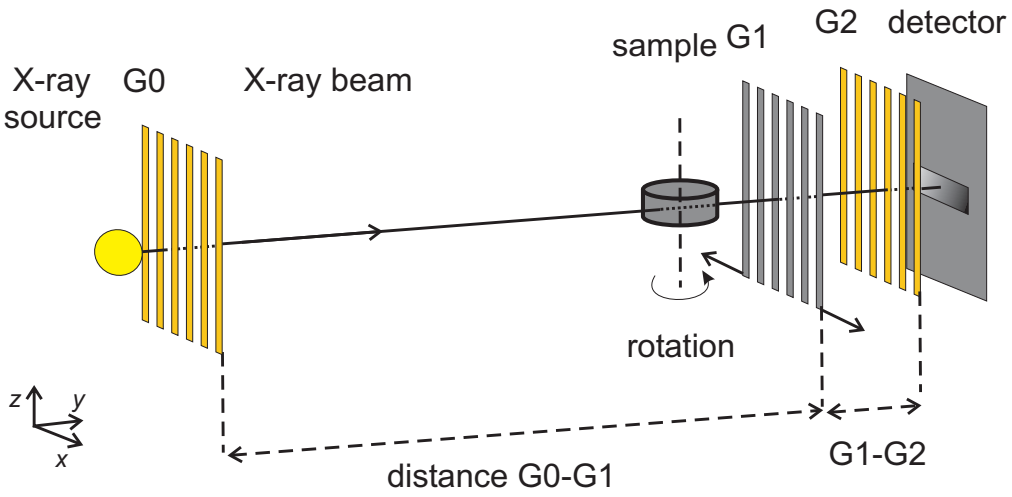

Fig. 1. X-ray grating interferometer for differential phase-contrast imaging. A phase object in the beam path causes a slight deflection of x-rays changing the locally transmitted intensity through the arrangement formed by the gratings G1 and G2. The sample is placed on a tomographic rotation stage.

As x-ray source we used a Seifert ID 3000 x-ray generator operated at 40 kV and 25 mA with a tungsten (W) line focus tube (DX-W8 $\times$ 0.4-L). Due to the inclination of the target with respect to the optical axis of 6°, the effective source size was 0.8 (h)$\times$ 0.4 (v)mm^2. A PILATUS 100K pixel detector consisting of an array of 487$\times$195 pixels with a pixel size of 0.172 $\times$ 0.172 mm^2 was used to record images. Its detection efficiency determined by the probability of absorbing an x-ray in the 320- m-thick Si sensor is $\sim$10% at 28 keV.

The measurements were carried out at room temperature in a water tank (of PMMA, 50 mm thick) filled with demineralized water. The water tank, with the fluid phantom hanging into it from the top, was placed in front of the G1 grating, with the cylindrical tubes of the phantom parallel to the rotation axis z (compare Fig. 1). For the tomographic scan 361 projections were taken for projection angles from $\Theta = 0°$ to 360°. For each projection 16 phase steps were

#108621 - $15.00 USD Received 11 Mar 2009; revised 18 Apr 2009; accepted 30 Apr 2009; published 29 May 2009

recorded with an exposure time of 10 seconds per image.

To obtain the phase-contrast and the conventional projection, a set of raw images was recorded for different positions of the grating G1. From this so-called phase-stepping scan (described in more detail in [6]) both projections were computed. These projections can directly be used as input for the filtered back-projection reconstruction algorithms, i.e., numerical implementations of Eqs. (5) and (6). Since our measurement was carried out in a water tank, we denote the reconstructed x-ray attenuation coefficients as Δ (x,y) and the measured refractive index decrements as $\Delta\delta(x,y)$ to indicate that these values give the difference to the respective values of water.

The calculation of theoretical values for and δ for each fluid was performed using their density at room temperature [26] and their elemental weight fractions, both listed in Table 1. In the following we denote calculated values by an index 'c' e.g. as $_c$ and δ_c. For the dilution series of NaCl in water the density as a function of salt concentration was used in the calculation. Since we could not find tabulated data for the density of the dilution series of NaI in ethanol and for the ethanol-glycerol mixtures, consequently we did not calculate theoretical values for these mixtures. To calculate δ_c we used tabulated data of Kissel [27] and for the calculation of $_c$, we used the data of Plechaty et al. [29]. Since our measurements were carried out in a water tank, i.e. relative to water, we give the theoretical values relative to those of water as $\Delta_c = _c - _c(\mathrm{H_2O})$ and $\Delta\delta_c = \delta_c - \delta_c(\mathrm{H_2O})$ for comparison with the experimental results.

Both and δ strongly depend on the x-ray energy. For the comparison of measured and calculated values we thus have to select an effective photon energy, for which we calculate the theoretical data. The measurement of and δ is generally carried out with two different effective x-ray energies due to two main reasons: 1.) The image formation processes of the conventional and the phase-contrast data are intrinsically different, and 2.) the specific energy-dependent efficiency of the x-ray optical gratings leads to a different weighting of the initial energy spectrum (for more details, see [30, 31]). Thus, we use two different effective x-ray energies E and E_δ, which we determine from the measured data of ethanol as described below since we used a photon-counting but not energy despersive detector for the measurements.

3. Results and discussion

Reconstructions of Δ and $\Delta\delta$ from the same slice of the phantom are shown in Figs. 2(a) and 2(b), respectively. For the specific reconstructions shown in Fig. 2, 55 tomographic slices were averaged (along the z-axis) to increase the signal-to-noise ratio. From these reconstructions experimental values for Δ and $\Delta\delta$ were determined from the mean value over a circular averaging region of 30 pixels diameter (containing 709 pixels) within each tube. Also the standard deviations σ and σ_δ over all pixels were determined. The measured values together with the standard deviations are given in Table 2. Figure 3 shows a scatter plot of the measured Δ and $\Delta\delta$ values.

The tube with demineralized water in the phantom serves as a control of the zero value. Water should be measured as zero, since the measurement was carried out in a water tank, i.e., relative to water. We find that the measured values for water $\Delta = 0.023 \pm 0.019 \cdot 10^{-2}\mathrm{mm}^{-1}$ and $\Delta\delta = -0.015 \pm 0.049 \cdot 10^{-8}$ fall approximately within one standard deviation from zero. A second very important result is the fact that the measured values for Δ and $\Delta\delta$ change in the correct proportion depending on the concentration for all three fluid series H_2O-NaCl, EtOH-NaI, and EtOH-Gly.

Effective energies for the and the δ measurements were determined by matching the measured and the calculated data for ethanol, which has comparitively large signals in both and δ. The minimum difference between measured and calculated values was obtained for $E = 30.1$ keV and $E_\delta = 28.3$ keV, both determined with 0.1 keV resolution. Note that both effective en-

#108621 - $15.00 USD Received 11 Mar 2009; revised 18 Apr 2009; accepted 30 Apr 2009; published 29 May 2009

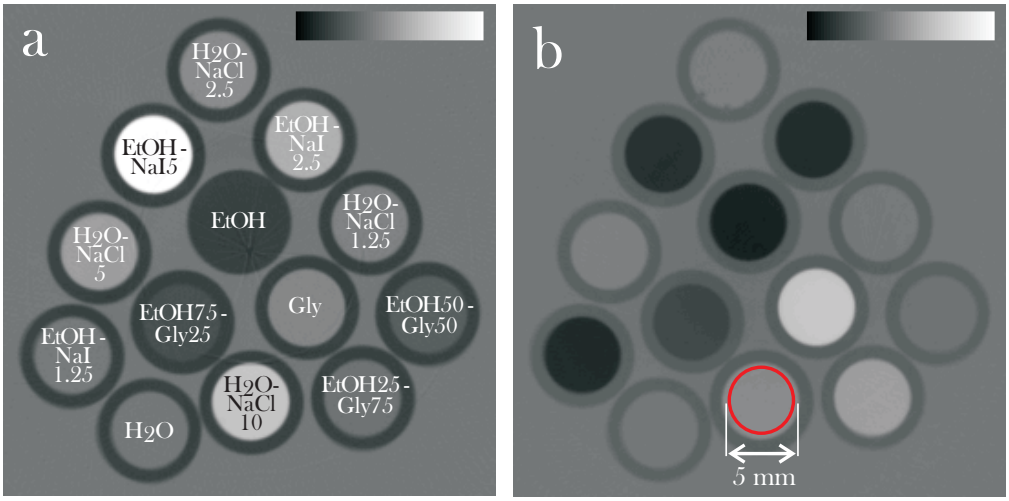

Fig. 2. Tomographic reconstructions from the same slice of the phantom showing **(a)** the attenuation coefficient $\Delta\ (x,y)$ and **(b)** the refractive index decrement $\Delta\delta(x,y)$. The color-bar (from black to white) ranges from -2.0 $\cdot 10^{-2}$ to 3.0 $\cdot 10^{-2}$ mm^{-1} in (a) and from -7.5 $\cdot 10^{-8}$ to 11.3 $\cdot 10^{-8}$ in (b). The fluids in the 13 polyethylene tubes of the phantom have been labeled with their identifiers according to the fluid description in Table 1. A centered, circular averaging region, as shown for one tube in (b), was defined for each tube to obtain the experimental values given in Table 2.

ergies and especially E_δ are close to the interferometer design energy of 28 keV. Using these effective energies we observe that for most fluids the measured values closely match the theoretically calculated values. Only the fluids with high and δ values (H_2O-NaCl5, H_2O-NaCl10 and Gly) show a trend to have too low measured δ values. This might be attributed to beam-hardening effects or to a slightly wrong effective energy E_δ due to error in the ethanol measurement that was used for the determination of the effective energies.

From the reconstructions in Fig. 2 and the plot in Fig. 3 it is obvious, that fluids can be much better distinguished by using both complementary signals instead of only one. Here we are interested in the contrast between two fluids in the absorption and the phase-contrast signal. Contrast can be described by the contrast-to-noise ratio

$$\mathrm{CNR} = \frac{|S_a - S_b|}{\sigma_S}, \tag{7}$$

where S_a and S_b represent the measured signals Δ (or $\Delta\delta$) of fluids a and b, respectively, and $\sigma_S = (\sigma_a^2 + \sigma_b^2)^{1/2}$ is the standard deviation of the signal difference $|S_a - S_b|$, with the standard deviation σ_a and σ_b of the respective signals. For example for the fluids H_2O-NaCl1.25 and glycerol (Gly) we find CNR = (0.358-0.247)/(0.022^2+0.028^2)$^{1/2}$ = 3.12 looking at the attenuation coefficients, but looking at the refractive index decrements instead, we find a much higher contrast-to-noise ratio of CNR_δ = (5.831-0.122)/(0.077^2+0.053^2)$^{1/2}$ = 61.07. Similarly, we find for the fluids H_2O and EtOH-NaI1.25 contrast-to-noise ratios of CNR = 1.44 and CNR_δ = 70.16. These substances can thus hardly be distinguished by their attenuation coefficients alone, but easily by looking at their refractive index decrements. Vice versa, the fluids EtOH and EtOH-NaI1.25 show less contrast for the refractive index decrement (CNR_δ = 4.79) than for the attenuation coefficient (CNR = 22.04), but can be easily distinguished by looking at both complementary signals.

#108621 - $15.00 USD Received 11 Mar 2009; revised 18 Apr 2009; accepted 30 Apr 2009; published 29 May 2009

Table 2. Measured and calculated attenuation coefficients Δ and refractive index decrements $\Delta\delta$ for all fluids in the phantom (relative to water). The standard deviations σ and σ_δ within each averaging region are given. The calculated Δ_c and $\Delta\delta_c$ values were determined for effective photon energies of $E = 30.1$ keV and $E_\delta = 28.3$ keV, respectively, as discussed in the text. The data is plotted in Fig. 3.

Identifier	$\Delta \pm \sigma$ $[10^{-2}/mm]$	$\Delta_c(E)$ $[10^{-2}/mm]$	$\Delta\delta \pm \sigma_\delta$ $[10^{-8}]$	$\Delta\delta_c(E_\delta)$ $[10^{-8}]$
H_2O	0.023 ± 0.019	0	-0.015 ± 0.049	0
Gly	0.358 ± 0.022	0.382	5.831 ± 0.077	6.736
EtOH	-1.220± 0.054	-1.219	-5.632 ± 0.076	-5.634
H_2O-NaCl1.25	0.247 ± 0.028	0.201	0.122 ± 0.053	0.208
H_2O-NaCl2.5	0.467 ± 0.022	0.406	0.486 ± 0.022	0.413
H_2O-NaCl5	0.878 ± 0.028	0.827	0.662 ± 0.028	0.829
H_2O-NaCl10	1.796 ± 0.018	1.707	1.388 ± 0.028	1.670
EtOH-NaI1.25	0.065 ± 0.022	–	-5.183 ± 0.055	–
EtOH-NaI2.5	1.272 ± 0.028	–	-5.013 ± 0.045	–
EtOH-NaI5	3.539 ± 0.038	–	-4.782 ± 0.038	–
EtOH75-Gly25	-0.906 ± 0.027	–	-3.361 ± 0.066	–
EtOH50-Gly50	-0.540 ± 0.025	–	-0.340 ± 0.042	–
EtOH25-Gly75	-0.115 ± 0.017	–	2.767 ± 0.044	–

4. Conclusions

Our results clearly illustrate that PC-CT as a combined CT method, which simultaneously yields phase-contrast and attenuation-contrast images, provides significantly more and unique information than any of the techniques alone. We have particularly shown that our approach can yield quantitative volume information of the distribution of the refractive index decrement δ and the attenuation coefficient . By combining both signals, the absorption and the phase-contrast signal, it is possible to distinguish substances with weak contrast in either one of the signal channels and to generally improve the specificity of the measurement using the second signal provided in PC-CT. The presented experimental results obtained from a self-built fluid phantom agree well with the theoretical expectation. In particular because of the quantitativeness of the results, demonstrated with a conventional polychromatic x-ray tube source, we believe that this method is of great interest for a wide range of quantitative x-ray CT applications, including future medical diagnostics, industrial non-destructive testing, and other research areas.

Acknowledgments

We would like to thank Anastasia Savouchkina and Patrick Farquet for their help in preparing the chemical solutions.

#108621 - $15.00 USD Received 11 Mar 2009; revised 18 Apr 2009; accepted 30 Apr 2009; published 29 May 2009

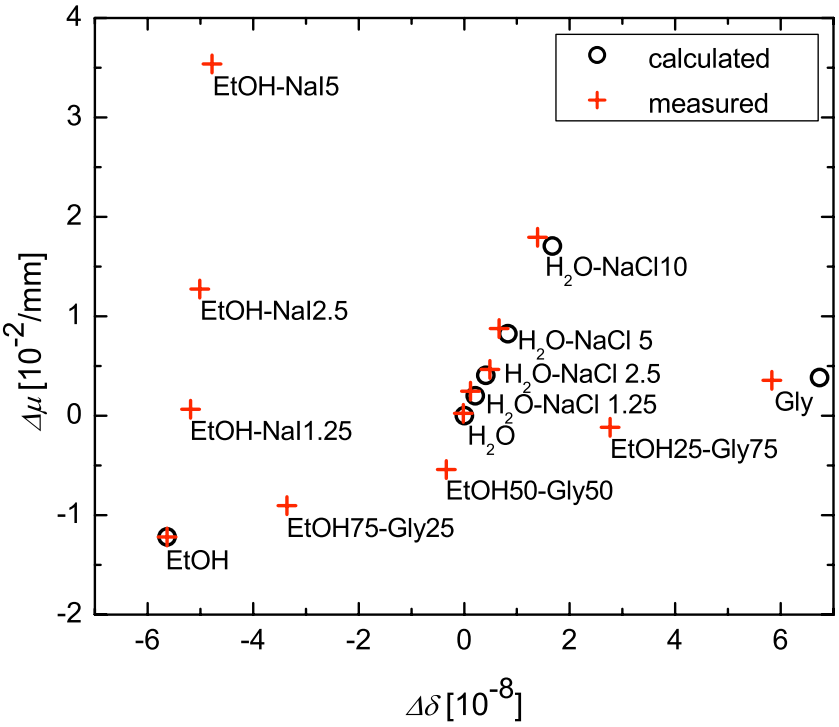

Fig. 3. Scatter plot of measured and calculated attenuation coefficients Δ , Δ $_c$ and refractive index decrements $\Delta\delta$, $\Delta\delta_c$. The plot shows the data given in Table 2.

#108621 - $15.00 USD Received 11 Mar 2009; revised 18 Apr 2009; accepted 30 Apr 2009; published 29 May 2009